NUMERICAL SIMULATION OF THE T-SHAPE FILLET WELDS OF 304 AND 1020 STEEL PLATES

Farid VAKILI-TAHAMI[1], Peyman MAJNOUN[2], Navid AKHLAGHIFAR[3]

In this paper, the role of major parameters and material properties which affect the quality of weld, temperature distribution and displacement of T-shape fillet welded joints have been investigated. Two AISI 304 and AISI 1020 plates are used and temperature distribution and displacement of the certain points in the weldments have been recorded during the welding process by a computerized data processing system. These data are compared with the results of numerical simulation and good agreement has been observed. Results show the effect of the major factors: material conductivity, plate thickness, input heating and welding speed.

Keywords: Welding, Numerical simulation, Experimental study, Displacement, Temperature distribution, Stainless steel 304, Carbon steel 1020.

1. Introduction

Welding is a reliable and efficient metal joining process in almost all industries. This process is extensively used in various engineering applications such as constructions, ship building, automobile and pressure vessels. Generally, welding quality is directly influenced by the welding input parameters during the process. Welding quality is a general concept and hard to define because of differenet aspects which maybe concerned. However, as a basic criteria, mixing the melted filler metal with the parent material along the fusion boundary can be regarded as an option for controling the weld quality. The non-uniform expansion and contraction of the regions near the weld line, due to the heating and cooling cycles during the welding process, lead to thermal stresses [1-3]. Also, fillet-welded joints usually suffer from deformation that it has adverse effects on the accuracy, external appearance, service life and strengths of the welded structures. Prediction of the temperature fields during the welding process and cooling periods is a difficult task due to the complexity involved. Hence, the numerical methods such as finite element have gained a considerable popularity in the last three decades [4-6]. Due to the complexity of the welding process, the

[1] Associate Prof., Dept. of Mech. Eng., University of Tabriz, Iran, e-mail: f_vakili@tabrizu.ac.ir
[2] Dept. of Mech. Eng., University of Tabriz, Iran, e-mail: p.majnoon92@ms.tabrizu.ac.ir
[3] Dept. of Mech. Eng., Universityof Tabriz, Iran, e-mail: akhlaghi.navid93@ms.tabrizu.ac.ir

experimental measurements are costly, in spite of this fact they are necessary and required to develop any reliable numerical model.

Kong et al. [7] have investigated the mechanical behavior of spot-welded joints of steel using finite element methods. The effect of gas metal arc welding (GMAW) parameters such as welding voltage, welding speed and current on three responses (bead width, bead height and penetration) for optimization purposes of AS 1204 mild steel plate joints are studied by Kim et al. [8]. Sathiya et al. [9] have investigated the weld bead geometry such as depth of penetration, bead width and tensile strength of the laser welded butt joints made of AISI 904L super austenitic stainless steel. M. Mahapatraet et al. [10] have highlighted the effects of submerged arc welding process parameters on the temperature distribution and displacement of the welded joints. The three-dimensional welding simulations based on the commercial finite element analysis (FEA) software have been reported by Tekriwal and Mazumder [11, 12], Brown and Song [13], Michaleris and DeBiccari [14], Dong et al. [15], and Chao et al. [16].

Review of the research works reveal that the effect of material properties especially thermal conductivity of steels hasn't been considered in detail knowing that it has major role in welding process. Also, it is necessary to validate the models using experimental data. However, most of the models use too many empirical constants which require a lot of experimental data to calibrate. In this paper, the effect of material properties and welding parameters have been investigated on welding quality, temperature distribution and displacements of the T-shape fillet weld of AISI 304 stainless steel and AISI 1020 carbon steel plates. Because of their superior mechanical and corrosion properties, stainless steel 304 and carbon steel 1020 are used widely in the above-mentioned industries especially power generation and petrochemical plants. Experimental data are used to develop and validate the simulation of the welding process which has been carried out based on a modified Double-Ellipsoidal Heat Source (DEHS). Temperature distribution and displacement of the certain points have been recorded during the welding process using a data logger system. Results indicate that the major factors which affect the temperature distribution around the weldment are thermal conductivity, thickness, input heating and welding speed.

2. Experimental procedure

Experimental tests have been carried out on T-shape fillet-weld joints of AISI 304 stainless steel and AISI 1020 carbon steel plates with 5, 6 and 8mm thicknesses. It is noticeable that carbon steel has the highest thermal conductivity (about 54 W/m °C) and stainless steel has the minimum value (about 12 W/m °C) among the industrial and commonly used steels. The chemical compositions and thermo-physical and mechanical properties for these metals are shown in Table 1

and Table 2, respectively. It can be seen that the trend of the change of thermal conductivity with temperature is different for these two alloy steels; with increasing temperature, the conductivity increases for AISI 304 and decreases for AISI 1020 [17].

Table 1

Chemical composition of the steels

Wt.% of component	C	Cr	Mn	Ni	P	S	Si
AISI 304	0.06	18	1.95	8.9	0.02	0.01	0.4
AISI 1020	0.2	0.03	1.03	-	0.04	0.05	0.2

Table 2

The average values of temperature-dependent thermo-physical and mechanical properties for AISI 304 [18, 20] and AISI 1020 [19]

Temperature (^{0}C)	Specific heat (J/g °C)		Conductivity (W/mm °C)		Density (g/mm^3)		Yield stress (MPa)		Young modulus (GPa)		Poisson's ratio	
	AISI 304	AISI 1020	AISI 304	AISI 1020	AISI 304	AISI 1020	AISI 304	AISI 1020	AISI 304	AISI 1020	AISI 304	AISI 1020
0	0.462	0.480	0.0146	0.060	0.790	0.785	265	380	198.5	210	0.294	0.294
100	0.496	0.500	0.0151	0.050	0.788	0.785	218	340	193.0	200	0.295	0.295
200	0.512	0.520	0.0161	0.045	0.783	0.780	186	315	185.0	200	0.301	0.301
400	0.525	0.650	0.0179	0.038	0.779	0.776	170	230	176.0	170	0.310	0.310
600	0.540	0.750	0.0180	0.030	0.775	0.760	155	110	167.0	80	0.318	0.318
800	0.577	1	0.0208	0.025	0.766	0.752	149	30	159.0	35	0.326	0.326
1000	0.604	1.2	0.0239	0.026	0.756	0.739	91	25	151.0	20	0.333	0.333
1200	0.676	1.4	0.0322	0.028	0.737	0.730	25	20	60.0	15	0.339	0.339
1400	0.692	1.6	0.0337	0.037	0.732	0.725	21	18	20.0	10	0.342	0.342
1500	0.700	1.7	0.120	0.037	0.732	0.718	10	15	10.0	10	0.388	0.388

Due to the vast applications, Manual Metal Arc Welding (MMAW) process is employed in the experiments and plates are welded by one pass welding method. MMAW is usually used in "on-site" industrial applications, because the equipment is relatively simple, portable, and inexpensive. Welding direction is along the lamination and the plates are separate but tack welded before welding. The major dimensions of the plates (length 160mm; breadth of the flange 72mm; height of the web 72mm) are illustrated in Fig.1. The ''AWS 308L-17" and "AWS E7018" rutile coated core wire electrodes with 2.5 mm diameter are used for AISI 304 and AISI 1020 plates, respectively. These type of electrodes for welding of AISI 304 and 1020 are recommended by AWS A5.4/A5.4M standard [21].

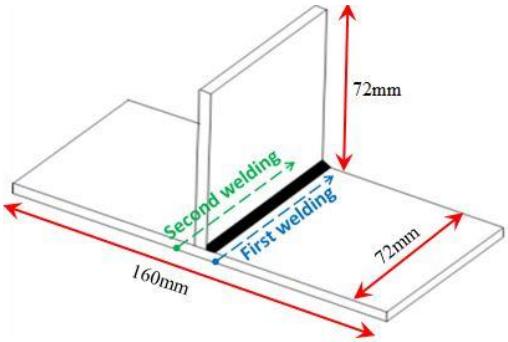

Fig. 1. T-shape joint and dimensions of the plates, the welding is along the lamination

Temperature and displacement histories are measured continuously during the welding and cooling periods, using an online data acquisition system with computer interface. This data logger (Fig.2a) uses “K type” thermocouples and is capable of recording up to 10 temperatures in each second. Thermocouples were fixed at the lower surface of the web plate in the specific points for temperature measurements along the welding line (Fig. 2c).

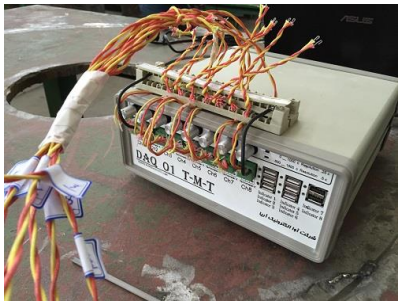

(a)

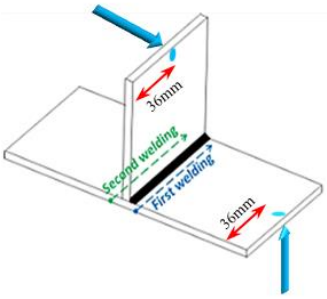

(b)

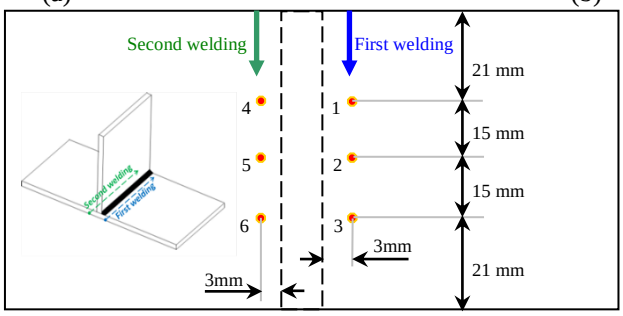

(c)

Fig. 2a) Data logger system
Fig. 2b) Location of the micrometers at the flange and web plates
Fig. 2c) Locations of the thermocouple joint-points at the lower surface of the main plate

The displacement of two edges of the flange and web plates are also continuously measured using two micrometers with the accuracy of ±0.01 mm which are located on the certain points according to Fig. 2b. The former measurements are used to validate the thermal solutions, whereas the later measurements are employed to validate the mechanical solutions of the model.A number of tests have been carried out at the same condition to provide a set of data for each case study. The welding parameters including the variation ranges of the current and voltage are measured during the welding process and are given in Table 3. This table lists the normal welding conditions for both materials, however; later, to study the effect of some parameters, these conditions are changed.

The schematic diagram of the setup and experimental test rig for T-shape weld joint plates are shown in Fig. 3. Further details of the experimental tests and its procedures have been reported in references [6].

Table 3

The normal welding conditions for AISI 304 and AISI 1020 plates with different thicknesses

Case No.	Material of plate	Plate thickness (mm)	Current (A)	Voltage (V)	Welding speed (mm/sec)	Length of leg (mm)
1	AISI 304	5	90 ± 3%	28 ± 4%	2.34	5
2	AISI 304	6	90 ± 3%	28 ± 4%	2.34	5
3	AISI 304	8	90 ± 3%	28 ± 4%	2.34	5
4	AISI 1020	5	103 ± 5%	24 ± 5%	1.75	5
5	AISI 1020	6	103 ± 5%	24 ± 5%	1.64	5
6	AISI 1020	8	103 ± 5%	24 ± 5%	1.37	5

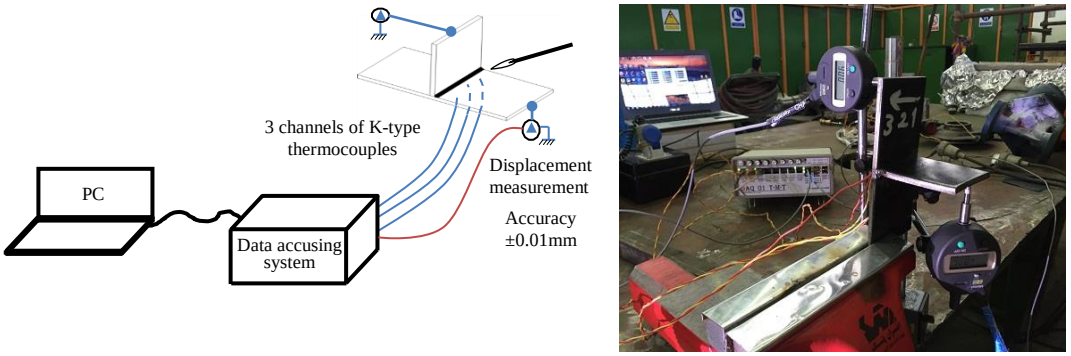

Fig. 3. Schematic diagram and experimental equipment of the test rig for data recording during the welding of T-shape joint plates

3. Finite element modeling

In this study, the simulation of the T-joint weld plates are performed by a three dimensional model developed in ANSYS. A modified Double-Ellipsoidal

Heat Source (DEHS) is implemented to model the moving heat source. Also, the birth of the element technique is used to simulate the metal filler. Indirect or decoupled solution method is used to carry out the mechanical modeling. In other words, two consecutive solution stages are performed: one is the thermal analysis in which the temperature for each node is recorded at each time step. The output from the thermal analysis is then used to carry out mechanical elasto-plastic analysis in order to calculate the displacement, strains and the subsequent stresses.

The dimensions of the models are the same as the test specimens. In the finite element model, 121045, 167486 and 214817 are the number of nodes which have been used for 5, 6 and 8 mm-thicknesses, respectively. In the thermal analysis, eight node elements (known as Solid-70 in ANSYS manual) with a single degree of freedom (temperature) are used [6]. In order to predict the thermal histories more accurately, at the weld zone and its proximity, a fine mesh is adopted. Fig. 4 shows the finite element mesh model with its element for 6 mm-thickness plates.

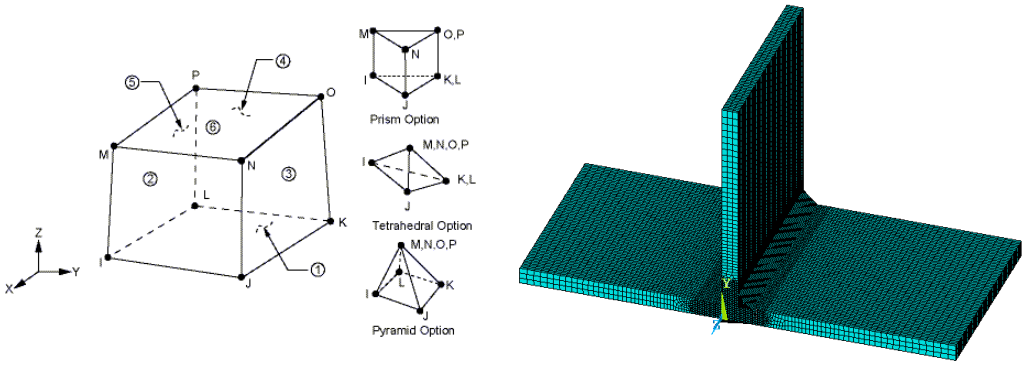

Fig. 4. Finite element model by Solid-70 element for the fillet weld of 6mm-thickness plates

3.1. Thermal analysis

The governing equation for transient heat transfer analysis during the welding process is given by [18]:

$$\rho c \frac{\partial T}{\partial t}\left(x,y,z,t\right) = -\nabla.\vec{q}\left(x,y,z,t\right) + \mathrm{Q}\left(x,y,z,t\right) \tag{1}$$

in which, ρ is the density of the materials, c is the specific heat capacity, T is the current temperature, t is time, x, y and z are coordinates in the reference system, $\vec{q}$ is the heat flux vector and Q is the internal heat generation rate, and ∇ is the spatial gradient operator. The non-liner isotropic Fourier heat flux constitutive equation is employed:

$$\vec{q} = -k\nabla T \tag{2}$$

where k is the temperature-dependent thermal conductivity.

Considering the effect of welding speed, the power density should be asymmetrically distributed ahead of the arc and behind it. In this study, the heat from the moving welding arc is applied as a volumetric heat source with a double ellipsoidal distribution proposed by Goldak et al. [22]. They have proposed the double-ellipsoid heat source (DEHS) which has been often used to approximate the heat source in common non-autogenous welding processes. The DEHS is expressed by the following equations for the front and rear of the welding center:

$$q_f\left(x,y,z\right)=\frac{6\sqrt{3}}{\pi\sqrt{\pi}}\ \frac{I\times V\times\eta\times f_f}{abc_f}e^{-3\left\{\frac{x^2}{a^2}+\frac{y^2}{b^2}+\frac{\left(z-vt\right)^2}{c_f{}^2}\right\}} \tag{3}$$

$$q_r\left(x,y,z\right)=\frac{6\sqrt{3}}{\pi\sqrt{\pi}}\ \frac{I\times V\times\eta\times f_r}{abc_r}e^{-3\left\{\frac{x^2}{a^2}+\frac{y^2}{b^2}+\frac{\left(z-vt\right)^2}{c_r{}^2}\right\}} \tag{4}$$

In these equations, I is the electric current, V is the voltage and η is the efficiency of arc welding. Also, q_f and q_r denote the front and rear heat flux distributions respectively, f_f and f_r are parameters which give the fraction of the heat deposited in the front and the rear parts, respectively. The v parameter is welding speed and a, b, c_f and c_r are the radius of the rear and front ellipsoid. For the front part of the semi-ellipsoid, the heat deposition is:

$$2\int_0^\infty\int_0^\infty\int_0^\infty q_f(x,y,z)dxdydz=2\times\frac{6\sqrt{3}}{\pi\sqrt{\pi}}\frac{Q.f_f}{abc_f}\int_0^\infty e^{-3\left\{\frac{x^2}{a^2}+\frac{y^2}{b^2}+\frac{z^2}{c_f{}^2}\right\}}dxdydz=\frac{1}{2}Q.f_f \tag{5}$$

Similar integration can be carried out for the rear part.

Since $Q=\eta IV=0.5Q\left(f_f+f_r\right)$, then $f_f+f_r=2$. In this study, the parameters of f_f and f_r are assumed to be 1.4 and 0.6, respectively, because the temperature gradient in the front leading part is steeper than in the tailing edge [23]. The formulation of the DEHS to accurately model the T-shape joint steel plates based on MMAW process is modified by Vakili and Ziaei [6]:

$$q_f(x,y,z,t)=\lambda\frac{\eta IVf_f}{V_{WeldBead}}e^{\left\{\frac{\left[(x-x_0)+(y-y_0)\right]^2}{\left[c\times\sqrt{2}/2\right]^2}+\frac{\left[(x-x_0)-(y-y_0)\right]^2}{\left[c\times\sqrt{2}\right]^2}+\frac{(z-vt)^2}{\left[c\times\sqrt{2}\right]^2}\right\}(-3\cos^2\theta)};z>vt \tag{6}$$

$$q_r(x,y,z,t)=\lambda\frac{\eta IVf_r}{V_{WeldBead}}e^{\left\{\frac{\left[(x-x_0)+(y-y_0)\right]^2}{\left[c\times\sqrt{2}/2\right]^2}+\frac{\left[(x-x_0)-(y-y_0)\right]^2}{\left[c\times\sqrt{2}\right]^2}+\frac{(z-vt)^2}{\left[c\times\sqrt{2}\right]^2}\right\}(-3\cos^2\theta)};z<vt \tag{7}$$

where λ is a coefficient which is obtained based on experimental data and $V_{WeldBead}$ is the volume of weld bead. θ is the angle between x and x' according to Fig. 5.

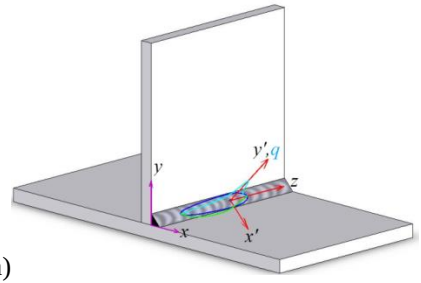

(a)

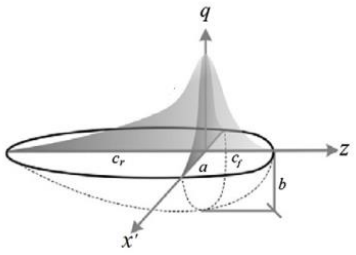

(b)

Fig. 5a. Transformation of the coordinate system
Fig. 5b. Representation of the parameters to define heat source

They have introduced a new set of coefficients (Table 4) related to the parameters of fusion zone to simulate the behavior of the moving heat source in the described arc welded T-shape joint. According to the welding conditions the parameters of the heat source can be adjusted to create a desired melted zone. The moving heat source is modeled by a user subroutine in ANSYS code.

Table 4

Coefficients for the modified numerical model [6]

λ	η	f_f	f_r	θ	c (mm)	a (mm)	b (mm)	c_f (mm)	c_r (mm)
0.4545	0.75	1.4	0.6	45°	5	$5\sqrt{2}/2$	$5\sqrt{2}$	$5\sqrt{2}$	$10\sqrt{2}$

To simulate the combined thermal boundary conditions, the effect of radiation at high temperatures and the effect of convection at lower temperatures have been considered. For thermal analysis of the welding processes, combined radiation and convective heat transfer coefficients have been used by many researchers [6, 24-26]. The Eq. (8) gives the total temperature-dependent heat transfer coefficient for both convection and radiation.

$$h=\begin{cases}0.0668T\left(\mathrm{W/m^2{}^\circ C}\right) & \text{when } T\le 500^\circ\mathrm{C}\\ \left(0.231T-82.1\right)\left(\mathrm{W/m^2{}^\circ C}\right) & \text{when } T\ge 500^\circ\mathrm{C}\end{cases} \tag{8}$$

These boundary conditions are employed for all free surfaces of the model.

3.2. Mechanical analysis

The finite element model employed for the mechanical analysis is similar to the thermal analysis with the exception of the elements type and boundary conditions. However, element-shape and number of nodes are the same. The mechanical analysis is carried out using the temperature histories computed by the

thermal analysis as the input data. During the welding process [18], the total strain rate can be decomposed into three components as follows:

$$\dot{\varepsilon} = \dot{\varepsilon}^e + \dot{\varepsilon}^p + \dot{\varepsilon}^{th} \tag{9}$$

Regarding to the components of the right hand side in the above equation, total strain can be divided into elastic strain, plastic strain and thermal strain, respectively. The elastic behavior is modeled using the isotropic Hook's rule with temperature-dependent Young's modulus and Poisson's ratio (see Table 2). The thermal strain is considered using the temperature-dependent coefficient of thermal expansion. For the plastic strain, a rate-independent plastic model is employed with the following features: the Von Mises yield surface, temperature-dependent mechanical properties, and linear isotropic hardening model [18].

4. Results and discussion

In this section, the results of numerical solutions are compared with the experimental measurements for the welding of plates with 5, 6 and 8 mm of thickness. Since the trend of the temperature variation for all case studies is the same, to avoid any confusion or repetition only results of 6 mm-thickness plates is presented in the figures. Fig. 6 and Fig. 7 show the comparison of the experimental measurements with the results of FE analysis as the thermal histories for the specific points on the back surface of the main plate (shown in Fig. 2c) during the welding and cooling periods for 6 mm thickness stainless steel and carbon steel plates, respectively. It can be seen that, there is a good agreement between experimental data and the results of numerical model.

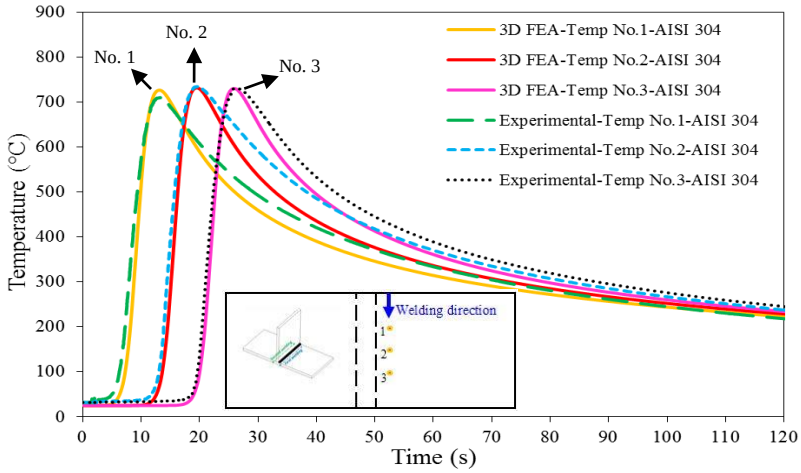

Fig. 6. Comparing the experimentally measured the maximum temperature levels and results for the numerical solutions during the welding and cooling periods for 6mm-AISI 304 plate

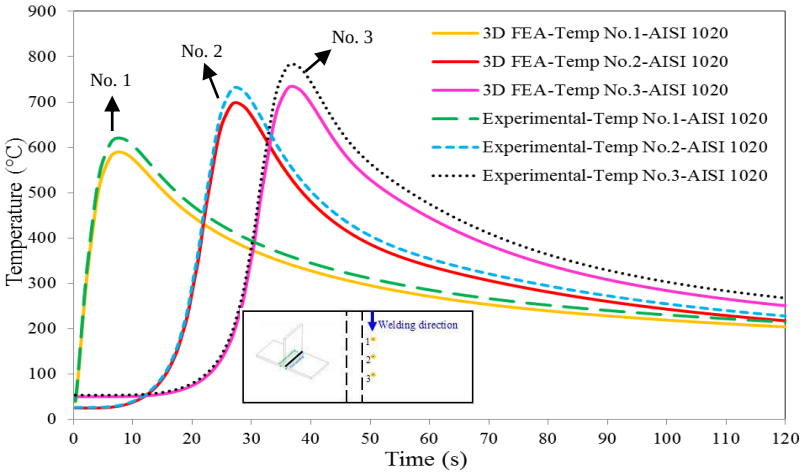

Fig. 7. Comparing the experimentally measured the maximum temperature levels and results for the numerical solutions during the welding and cooling periods for 6mm- AISI 1020 plate

Since the welding process is MMAW, based on the skill of the welder, environment and other conditions, the measured temperatures change and therefore each case study four tests have been carried out. It has been found that the results of the numerical solution match well with the maximum values and they are compared in Figs. 6 and 7. Also, the average-measured temperature for point No. 2 is compared with the results of FE analyses for all case studies; also, the error percentages are presented in Table 5.

Table 5

Comparison of the average temperature at point No. 2 obtained using experiment measurement and numerical analysis

Material of plate	Plate thickness (mm)	Welding speed (mm/sec)	Temperature at point No. 2 (ºC)		Error percentage
			3D FEA	Experimental (average)	
AISI 304	5	2.34	893	733	17.91%
AISI 304	5	4.69	747	611	18.20%
AISI 304	6	2.34	725	603	16.82%
AISI 304	8	2.34	500	448	10.40%
AISI 1020	5	1.75	827	824	0.36%
AISI 1020	5	2.05	745	735	1.34%
AISI 1020	6	1.64	699	749	-7.15%
AISI 1020	8	1.37	501	540	-7.78%

Results depict that by increasing the weld speed from 2.34 to 4.69 mm/s (100% increase) for AISI 304 and from 1.75 to 2.05 mm/s (17% increase) for AISI 1020 in 5 mm plate, the temperature of point No. 2 decreases 20% and 11%, respectively. Also, by increasing the plate thickness to 8 mm, the temperature of

the same point reduces by 39% and 35% for AISI 304 and AISI 1020, respectively. It is noticeable that, due to the coefficient of thermal conductivity for AISI 304 (almost 12 W/m °C) and AISI 1020 (almost 54 W/m °C), the welding speed cannot be increased further to obtain the desired quality of the weld and fusion layer. The average temperature history of the weld bead (average temperature of point No. 1 to No. 4) which indicates the appropriate welding quality for both alloys is illustrated in Fig. 8. In other words, when the average temperature of the weld pool is less than 1500°C (melting point of the material) or when this temperature is more than 2500°C (vaporizing temperature of the material) the quality of the weld is regarded to be unacceptable.

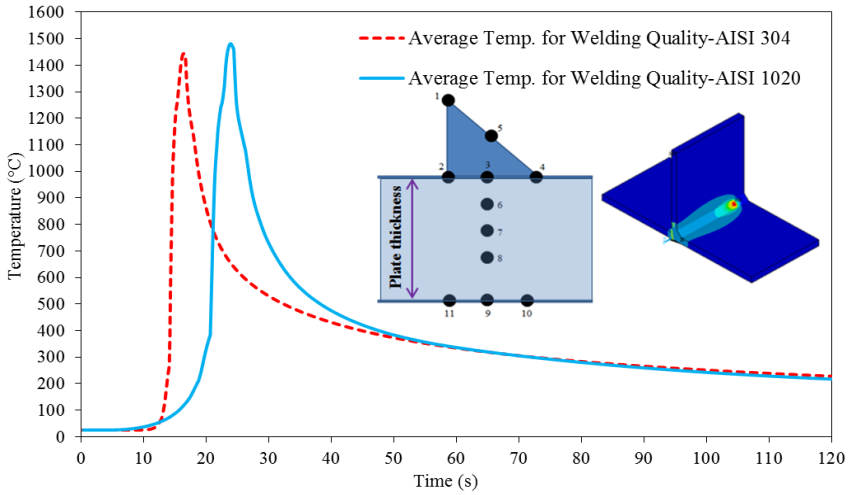

Fig. 8. Comparing the average temperature of the weld bead for 6mm-AISI304 and 1020

Based on the melting point of the stainless and carbon steel [27], welding conditions, which give “average weld bead temperature” higher than 1450°C can be regarded as welds with acceptable quality and with good penetration. As an example the results for an acceptable weld are shown in Fig. 8 for both alloys. Also, the associated welding conditions are given in Table 3.

Carbon steel and stainless steel have higher and lower bounds of the thermal conductivity in commercial industrial steels. Due to this range in coefficient of thermal conductivity which is a major factor in the heat transfer process, welding parameters such as welding speed, maximum temperature (for example point No. 2 shown in Fig. 2c), and average weld bead temperature are different for two alloys. Also, the thickness of the plate has a significant effect on these parameters. Due to these complex interrelations of the parameters, experimental study of the welding condition will be expensive and time consuming. Hence, numerical solutions are used to predict above-mentioned

parameters to provide an instruction table such as Table 6 to help in determining appropriate welding condition.

Table 6

The effect of welding parameters on quality of weld and maximum temperature at point No.2 using numerical analysis

Case No.	Material of plate	Plate thickness (mm)	Welding speed (mm/sec)	Heat input ($Q=\eta \times I \times V$) (Watt)	Average weld bead temp. (ºC)	Maximum temperature at point No. 2 (ºC)
1	AISI 304	5	2.34	1890	1479	893
2	AISI 304	5	4.69	1890	1406	747
3	AISI 304	5	2.34	2174	1601	1012
4	AISI 304	5	2.34	2363	1674	1081
5	AISI 304	6	2.34	1890	1447	725
6	AISI 304	6	4.69	1890	1428	687
7	AISI 304	6	2.34	2174	1572	824
8	AISI 304	6	2.34	2363	1645	884
9	AISI 304	8	2.34	1890	1429	500
10	AISI 304	8	2.34	2174	1549	569
11	AISI 304	8	2.34	2363	1622	612
12	AISI 1020	5	1.75	1854	1500	827
13	AISI 1020	5	2.05	1854	1414	745
14	AISI 1020	5	1.75	2132	1643	951
15	AISI 1020	5	1.75	2318	1722	1039
16	AISI 1020	6	1.64	1854	1490	699
17	AISI 1020	6	1.92	1854	1452	639
18	AISI 1020	6	1.64	2132	1526	720
19	AISI 1020	6	1.64	2318	1611	771
20	AISI 1020	8	1.37	1854	1445	501
21	AISI 1020	8	1.6	1854	1400	464
22	AISI 1020	8	1.37	2132	1599	563
23	AISI 1020	8	1.37	2318	1684	609

The results of numerical solution for mechanical analysis are compared with the experimental data to assess the accuracy and the reliability of the simulation in predicting the mechanical behavior of the weldment. For this purpose the deformation of plate edges measured during the welding process and cooling periods are compared with the results obtained using numerical solution. Since in the FE analysis, stresses and strains are obtained from resulting displacement values, the good agreement of the displacements with the test data ensures the accuracy of the simulation.

Fig. 9 compares the displacement at the edge of the flange plate for FE mechanical analysis and experimental measurements for 6 mm plates. There are good agreements between experiment tests and numerical simulations. It can be seen that the displacement of the carbon steel plate is much less than the stainless steel plate. This is due to the fast heat dissipation rate in the carbon steel plates.

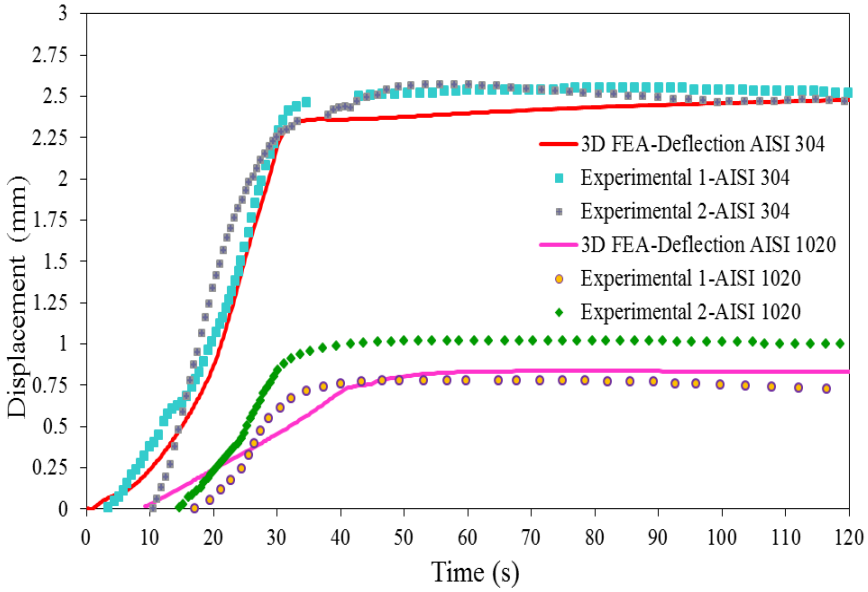

Fig. 9. Comparing the measured maximum displacement at the edge points of the plates during the welding and cooling periods and those calculated using numerical analysis for 6mm-thickness AISI 304 and AISI 1020

In Table 7, the maximum displacements at the edge points of the flange plate which are calculated from numerical analysis are compared with the experimental measurements. As it can be seen in this table, the difference between numerical results and experimental measurements is less than ten percent. Considering the accuracy of the measuring devices, which are within this limit, and complexity of the welding process, this difference limit is acceptable in engineering applications and therefore, it can be concluded that the FE based mechanical model has acceptable accuracy.

Table 7

Comparison of the maximum displacement at the edge points obtained in experimental measurements and numerical analysis

Material	Plate thickness (mm)	Welding speed (mm/sec)	Maximum displacement (mm)		Error percentage
			3D FEA	Experimental (average)	
AISI 304	5	2.34	2.36	2.53	-6.7%
AISI 304	6	2.34	2.4	2.66	-9.7%
AISI 304	8	2.34	2.4	2.43	-1.2%
AISI 1020	5	1.75	0.58	0.635	-8.6%
AISI 1020	6	1.64	0.84	0.9	-6.6%
AISI 1020	8	1.37	0.77	0.82	-6.1%

6. Conclusions

In this study, a 3D FE model is developed to analyze the thermo-mechanical behavior of the T-shape weldments such as temperature fields and the displacement variations during the welding and cooling periods. The results of the numerical solution have been compared with test data and good agreements have been observed. Also, the results show the very important role of the thermal conductivity of the materials. Two alloys: AISI 304 and AISI 1020 plates have been selected which provide lowest and highest levels of conductivity among the commercial steels. Although, results show that other parameters such as welding speed, heat input have significant effects but it is clear that all these parameters are selected according to the thermal conductivity to provide acceptable weld quality. The role of thermal conductivity becomes more significant when the plate thickness changes due to the increasing thermal resistance.

R E F E R E N C E S

[1]. *Özyürek, Dursun*, "An effect of weld current and weld atmosphere on the resistance spot weldability of 304L austenitic stainless steel", Materials & design, **vol. 29**, no. 3 (2008), pp. 597-603.

[2]. *Benyounis, K. Y., and A. G. Olabi*, "Optimization of different welding processes using statistical and numerical approaches–A reference guide", Advances in engineering software, **vol. 39**, no. 6 (2008), pp. 483-496.

[3]. *Shanmugam NS, Buvanashekaran G, Sankaranarayanasamy K, Kumar SR*, "A transient finite element simulation of the temperature and bead profiles of T-joint laser welds", Materials & design, **vol. 31**, no. 9 (2010), pp. 4528-4542.

[4]. *H. D. Hibbitt , P. V. Marcal*, "A numerical, thermo-mechanical model for the welding and subsequent loading of a fabricated structure", Computers & Structures, **Vol. 3**, no. 5 (1973), pp. 1145-1174.

[5]. *D. Deng*, "FEM prediction of welding residual stress and distortion in carbon steel considering phase transformation effects", Materials & design, **vol. 30**, no. 2 (2009), pp. 359-366.

[6]. *Vakili-Tahami, F. and Ziaei-Asl, A.*, "Numerical and experimental investigation of T-shape fillet welding of AISI 304 stainless steel plates", Materials & design, **vol. 47**, (2013), pp. 615-623.

[7]. *X. Kong, Q. Yang, B. Li, G. Rothwell, R. English, X. Ren*, "Numerical study of strengths of spot-welded joints of steel", Materials & design, **vol. 29**, no. 8 (2008), pp. 1554-1561.

[8]. *Kim IS, Son KJ, Yang YS, Yaragada PKDV*, "Sensitivity analysis for process parameters in GMA welding processes using a factorial design method", Int. J. Mach. Tools Manuf., **vol. 43**, 2003, pp. 763-769.

[9]. *Sathiya, P., K. Panneerselvam, and MY Abdul Jaleel*, "Optimization of laser welding process parameters for super austenitic stainless steel using artificial neural networks and genetic algorithm", Materials & design, **vol. 36**, 2012, pp. 490-498.

[10]. *M. M. Mahapatra, G. L. Datta, B. Pradhan and N. R, Mandal*, "Three-dimensional finite element analysis to predict the ef-fects of SAW process parameters on temperature distribution and angular distortions in single-pass butt joints with top and bottom reinforcements", International Journal of Pressure Vessels and Piping, **vol. 83**, 2006, pp. 721-729.

[11]. *Tekriwal P, Mazumder J*, "Finite element analysis of three-dimensional transient heat transfer in GMA welding", Weld Journal, **vol. 67**, 1988, pp. 150-156.

[12]. *Tekriwal P, Mazumder J*, "Transient and residual thermal strain–stress analysis of GMAW", Journal of Engineering Material Technology, **vol. 113**, 1991, pp. 336-343.

[13]. *Brown S, Song H*, "Finite element simulation of welding of large structures", Journal of Engineering for Industry, **vol. 114**, 1992, pp. 441-451.

[14]. *Michaleris P, DeBiccari A*, "Prediction of welding distortion", Weld Journal, **vol. 76**, 1997, pp. 172-181.

[15]. *Dong Y, Hong JK, Tsai CL, Dong P*, "Finite element modeling of residual stresses in austenitic stainless steel pipe girth welds", Weld Journal, **vol. 76**, 1997, pp. 442-449.

[16]. *Chao YJ, Zhu XK, Qi X*, "WELDSIM—a welding simulation code for the determination of transient and residual temperature, stress and distortion. In: Atluri SN, Brust FW, editors", Advances in Computational Engineering and Science, **vol. 2**, 2000, pp. 1206-1211.

[17]. *J. Outinen, O. Kaitila, P. Mäkeläinen*, "High-temperature Testing of Structural Steel and Modelling of Structures at Fire Temperatures: Research Report", Helsinki University of Technology, 2001.

[18]. *D. Deng, H. Murakawa*, "Numerical simulation of temperature field and residual stress in multi-pass welds in stainless steel pipe and comparison with experimental measurements", Computational materials science, **Vol. 37**, No. 3 (2006), pp. 269-277.

[19]. *S. Nadimi, R. Khoushehmehr, B. Rohani, A. Mostafapour*, "Investigation and analysis of weld induced residual stresses in two dissimilar pipes by finite element modeling", Journal of Applied Sciences, **Vol. 8**, No. 6 (2008), pp. 1014-1020.

[20]. *K. Masubuchi*, "Analysis of welded structures: Residual stresses, distortion, and their consequences", Elsevier, 2013.

[21]. Specification for stainless steel electrodes for shielded metal arc welding. Document number: ANSI/AWS A5.4/A5.4M, American Welding Society; 2012.

[22]. *Goldak, J., Chakravarti, A. and Bibby, M.*, "A new finite element model for heat sources", J. Metall Trans B, **vol. 15**, 1984, pp. 299-305.

[23]. *D. Deng, Y. Luo, H. Serizawa, M. Shibahara, H. Murakawa*, "Numerical simulation of residual stress and deformation considering phase transformation effect", Trans. JWRI, **vol. 32**, No. 2 (2003), pp. 325-333.

[24]. *D. Deng, W. Liang and H. Murakawa*, "Determination of welding deformation in fillet-welded joint by means of numerical simulation and comparison with experimental measurements", Journal of Materials Processing Technology, **vol. 183**, 2007, pp. 219-225.

[25]. *E. Friedman*, "Thermo mechanical analysis of the welding process using the finite element method", Journal of Pressure Vessels Techno., **vol. 97**, No. 3(2010), pp. 206-213.
[26]. *S. A. A. A.Mousavi and R. Miresmaeili*, "Experimental and numerical analyses of residual stress distributions in TIG welding process for 304L stainless steel", Journal of Materials Processing Technology, **vol. 208**, 2008, pp. 383-394.
[27]. *Thorslund T, Kahlen FJ, Kar A*, "Temperatures, pressures and stresses during laser shock processing", J Optics Lasers Eng., **vol. 39**, No. 1 (2003), pp. 51-71.